Volume 1 | Number 1 | Jan 2013 | Pages 1–100

Journal of
Materials Chemistry A

Materials for energy and sustainability
www.rsc.org/materialsA

ROYAL SOCIETY
OF CHEMISTRY

ROYAL SOCIETY
OF CHEMISTRY

www.rsc.org/materialsA

ARTICLE TYPE

Complementary Solvent Additives Tune the Orientation of Polymer Lamellae, Reduce the Sizes of Aggregated Fullerene Domains, and Enhance the Performance of Bulk Heterojunction Solar Cells

Chih-Ming Liu,[a] Yu-Wei Su,[a] Jian-Ming Jiang,[a] Hsiu-Cheng Chen,[a] Shu-Wei Lin,[a] Chun-Jen Su,[b] U-Ser
5 **Jeng*[b,c] and Kung-Hwa Wei*[a]**

In this study we employed 1-chloronaphthalene (CN) and 1,8-diiodooctane (DIO) as binary additives
exhibiting complementarily preferential solubility for processing the crystalline conjugated polymer
10 poly[bis(dodecyl)thiophene-dodecyl-thieno[3,4-c]pyrrole-4,6-dione] (PBTC$_{12}$TPD) and the fullerene
[6,6]-phenyl-C$_{71}$-butyric acid methyl ester (PC$_{71}$BM) in chloroform. Using synchrotron grazing-incidence
small-/wide-angle X-ray scattering and transmission electron microscopy to analyse the structure of the
PBTC$_{12}$TPD /PC$_{71}$BM blend films, we found that the binary additives with different volume ratios in the
processing solvent allow us to tune the relative population of face-on to edge-on PBTC$_{12}$TPD lamellae
15 and size of PC$_{71}$BM clusters in the blend films; the sizes of the fractal-like PC$_{71}$BM clusters and the
aggregated domains of PC$_{71}$BM clusters increased and decreased, respectively, upon increasing the
amount of DIO; whereas the relative ratio of face-on to edge-on PBTC$_{12}$TPD lamellae increased upon
increasing the amount of CN. When fabricating the photovoltaic devices, the short-circuit current density
of the devices with the PBTC$_{12}$TPD/PC$_{71}$BM active layer having been processed with the binary additives
20 is higher than that of the device incorporating an active layer processed without any additive. As a result,
the power conversion efficiency of a device incorporating an active layer of PBTC$_{12}$TPD/PC$_{71}$BM (1:1.5,
w/w) processed with binary additives of 0.5% DIO and 1% CN in chloroform increased to 6.8% from a
value of 4.9%, a relative increase of 40%, for the corresponding device containing the same active layer
but processed without any additive.

1. Introduction

Solution-processed bulk heterojunction (BHJ) organic
photovoltaic devices based on composites of conjugated
polymers and nanometer-sized fullerenes are attracting great
attention because of their low cost, ease of fabrication, and the
30 potential for application in flexible devices.[1–7] Since the structure
of the BHJ active layer significantly influences the device
performance, the quest to develop an optimal active layer
morphology has led to testing of various processing parameters,
including annealing situations,[8] the solution casting conditions,
35 different solvents and solvent additives.[9–13] Moreover, the
changes in the active layer morphology with time also need to be
considered when designing polymer solar cells.[14] A BHJ layer
usually comprises a blend of donor (D), polymer, and acceptor
(A), fullerene, materials that organized into three phases: a
40 nanometer-scale phase-separated polymer phase, an aggregated
fullerene phase and a well inter-mixed polymer/fullerene phase.
The volume fractions of each of these three phases will depend
on the solvent used, the post processing conditions and the
additives incorporated during their processing, if any, and will
45 determine the optical and carrier transport properties of the active
layer.   These phases permit the absorption of different part of the

solar spectrum and play different important roles in the system;
the well inter-mixed polymer/fullerene phase gives efficient
exciton dissociation[15,16] at the polymer–fullerene interfaces, and
50 the phase-separated polymer and fullerene phase provide the
transport pathways of holes and electrons to their respective
electrodes, respectively. Our current understanding of the
structures of these three phases in crystalline polymer/fullerene or
amorphous polymer/fullerene[17,18] active layer morphologies
55 including their crystallization,[19] the extent of phase separation,
and solubility disparities[20] between the polymer and the fullerene
are qualitative at best; it arises essentially from the difficulty of
distinguishing the nanometer-scale phase separated materials that
both comprise mostly carbon atoms. Ideally, the electron donors
60 and acceptors form two respective intertwined continuous phases,
where the size of the domains will be approximately less than the
diffusion length of the exciton in the polymer domain (ca. 10
nm). The photogenerated excitons must diffuse to the D–A
interface in the active layer and dissociate prior to recombination
65 to effectively convert photon energy to electrical energy. The
development of a nanometer-scale morphology, which is
necessary to manufacture a high-performance organic
photovoltaics (OPV),[21,22] depends on the chemical composition of
the D and A components, the nature of the host solvent and
70 processing additives, and the post-processing treatment

conditions. Moreover, the device performances also critically depend on the contact of the active layer with the electrode.[23,24] The incorporation of solvent additives, which are placed into the solutions from which the BHJ layers are fabricated, is performed extensively when fabricating high-performance BHJ organic solar cells.[25–28] Typically, the solvent additive will have lower vapor pressure than that of the processing solvent and better solubility for the fullerene than for the polymer, allowing an elongated drying time for the active layer, in turn influencing the phase-separated morphology of the BHJ film and, therefore, improving the device performance. The use of a solvent additive, such as 1,8-diiodooctane (DIO),[29,30] 1-chloronaphthalene (CN),[31,32] or a conjugated molecule,[33] to control the morphology of the active layer is one of the simplest and most effective methods for optimizing the performance of a BHJ device.

In this study, we employed binary additives, DIO and CN, that have different relative solubility for the polymer and fullerenes as well as different boiling points to tune the active layer morphology; one additive improved the dispersion of the fullerene in the amorphous polymer phase because of its relatively better fullerene solubility,[11] as compared to the other one, while the other tune the orientation of the polymer lamellae, if any, because of its relatively better solubility for the polymer, as compared to the first one. Notably, the mechanism behind the packing of polymers in a face-on orientation in thin films has not been well understood.[34,35] Rather than covalently bonding fluorine atoms or linear alkyl chains to the polymer,[36,37] we incorporated binary additives into a processing solvent for inducing a greater face-on crystallite orientation relative to the substrate, thereby promoting hole transport toward the anode and inducing higher power conversion efficiency (PCE). Our approach provides a new mean of tuning the face-on orientation of polymer crystallites through variations in the nature and concentration of the binary additives.

Specifically, we varied the volume ratio of these two additives to influence the drying time of polymer/fullerene films as well as the relative solubility for the polymer and fullerene, thereby optimizing the morphology of the active layer and obtaining highly ordered lamellar sheets featuring a face-on orientation.[1,38–43] We used synchrotron grazing-incidence small- and wide-angle X-ray scattering (GISAXS and GIWAXS)[44–59] to analyze the orientation of the crystalline lamellae of the polymer with respect to the substrate[10,12,60–62] and the sizes of the fullerene aggregates.

We expect that the binary additives, DIO and CN, can reduce the size of the aggregated fullerene domains as well as tuning the orientation of the polymer lamellae such that the exciton dissociation and the pathways for carriers transport are improved. Because as the size of the aggregated fullerene domains is reduced owing to the decreased miscibility gap between the conjugated polymer and $PC_{71}BM$ induced by the binary additives, it indicates a larger volume fraction of intermixed polymer and fullerenes domains, which can be inferred from the photoluminescence (PL) and time-resolved (TR) PL spectroscopy study. As a consequence, we found that the PCE of a device incorporating poly[bi(dodecyl)thiophene-dodecyl-thieno[3,4-c]pyrrole-4,6-dione]   ($PBTC_{12}TPD$)/[6,6]-phenyl-C_{71}-butyric acid methyl ester ($PC_{71}BM$) (1:1.5, w/w) as the active layer improved from 4.9% when fabricated without any additive to 6.8% when processed with 0.5% DIO and 1% CN as additives in the processing solvent. Table 1 gives the solubility of $PBTC_{12}TPD$ and $PC_{71}BM$ in CF, DIO and CN.

Table 1. Solubility of $PBTC_{12}TPD$ and $PC_{71}BM$ in DIO, CN, and CF at room temperature, determined using ASTM E1148.

Additive	$PBTC_{12}TPD$ (mg mL^{-1})	$PC_{71}BM$ (mg mL^{-1})
DIO (b.p. = 333 °C)	1.4	21.7
CN (b.p. = 259 °C)	3.5	16.3
CF^a (b.p. = 61 °C)	4.5	21.6

^{a} From ref 10.

2. Experimental Section

2.1. Device fabrication

The synthesis of $PBTC_{12}TPD$ was reported elsewhere;[63] $PC_{71}BM$ was purchased from Solenne BV; chloroform (CF), DIO, and CN were obtained from Sigma–Aldrich. The Indium tin oxide (ITO), with a resistance 15 Ω, was obtained from Merck. ITO–coated glass substrates were sequentially cleaned with detergent, water, acetone, and isopropyl alcohol (ultrasonication; 10 min each), and then dried in an oven for 1 h; the substrates were treated with UV ozone for 15 min prior to use. A thin layer (ca. 30 nm) of polyethylenedioxy-thiophene:polystyrenesulfonate (PEDOT:PSS, Baytron PVP AI 4083) was spin-coated (4000 rpm) onto the ITO substrates. After baking at 140 °C for 20 min in air, the substrates were transferred to a N_2-filled glove box for deposition of the active layers from $PBTC_{12}TPD$/$PC_{71}BM$ mixtures at a weight ratio of 1:1.5 (30 mg mL^{-1}) in CF solutions at 60 °C, with or without processing additives (DIO: 0, 0.5, or 1 vol%; CN: 0, 0.5, or 1 vol%). In the design of these experiments, three different additive concentrations (0, 0.5, 1 vol%) for each of the two additives resulted in nine combinations for analyzing the mixing effects of DIO and CN. Here, we denote all the combinations with D_mC_n, with the subscripts m and n representing the volume percentages of the additives of D and C, respectively—in the processing solvent; for examples, $D_{0.5}C_{0.5}$ represents the device featuring an active layer comprising $PBTC_{12}TPD$ and $PC_{71}BM$ (1:1.5, w/w) that was processed with CF containing 0.5 vol % DIO and 0.5 vol % CN. The boiling points of CF, DIO, and CN are 61, 333, and 259 °C, respectively. The blend solutions with binary additives were spin-coated onto the PEDOT:PSS layers to from active layers having a thickness of approximately 300 nm. Devices were ready for measurements after thermal deposition (pressure: ca. 1×10^{-6} mbar) of a 20 nm-thick film of Ca and then a 100 nm-thick Al film as the cathode.

2.2. Device Characterization

Photovoltaic measurements of the devices were performed under simulated AM 1.5G irradiation (100 mW cm^{-2}) using a xenon lamp (Newport 66902, 150W solar simulator). The *J−V* characteristics were evaluated using a Keithley 2400 source meter. The active layers were immersed in DI water for exfoliation and then transferred to a Cu foil for image recording through transmission electron microscopy (TEM, *FEI Tecnai G2*) operated at 120 keV. External quantum efficiencies (EQEs) were recorded using a spectral response measurement set-up (Optosolar SR150).

GIWAXS/GISAXS measurements were performed to investigate the structure of the crystalline $PBTC_{12}TPD$ and the size of the aggregated $PC_{71}BM$ clusters, using the BL23A beamline station of the National Synchrotron Radiation Research Center (NSRRC) in Taiwan.[64] The BL23A beamline, equipped with a Pilatus 1M-F area detector for SAXS and a flat-panel C9728DK-10 area detector for WAXS, allowed simultaneous

GISAXS and GIWAXS measurements for correlated changes in crystalline structures and nanostructures in the same probing area of the thin films of interest. With the sample surface defined in the x-y plane and the incident x-rays in the x-z plane, the scattering wave vector transfer $q = (q_x, q_y, q_z)$ can be decomposed into three orthogonal components as follows: $q_x = 2\pi\lambda^{-1}(\cos\beta\cos\phi - \cos\alpha)$, $q_y = 2\pi\lambda^{-1}(\cos\beta\sin\phi)$, and $q_z = 2\pi\lambda^{-1}(\sin\alpha + \sin\beta)$, where α and β stand for incident and exit angles, respectively, and ϕ measures the scattering angle away from the y-z plane;[54,56,59] λ is the wavelength of the X-rays. The 8-keV X-ray beam used was 0.2 mm diameter, with a sample incident angle of 0.2°; the sample-to-detector distances were 5.0 and 0.25 m for the GISAXS and GIWAXS systems, respectively. The samples were prepared through spin-coating of PBTC$_{12}$TPD/PC$_{71}$BM solutions onto 4-cm^2 Si substrates; the film thickness was about the same for each sample (ca. 300 nm).

3. Result and Discussion

3.1 Molecular Structures and Characteristics

Figure 1a presents the molecular structures of the materials used in this study: PBTC$_{12}$TPD, PC$_{71}$BM, DIO, and CN. Figure 1b displays the UV–Vis absorption spectra of spin-coated PBTC$_{12}$TPD/PC$_{71}$BM thin films, processed with various amounts of the incorporated additives in the CF solvent for a similar thickness of approximately 300 nm. We attribute the minor absorption peaks at 375 nm and the major broad peaks at 550 nm to PC$_{71}$BM and PBTC$_{12}$TPD, respectively. The absorption peak intensity at 550 nm for the PBTC$_{12}$TPD/PC$_{71}$BM blend films, processed with the 0.5 vol% of the CN additive, was larger than that of the blend film processed without any additive; with 1 vol% CN, the peak intensity further increased slightly. With a distinct shoulder vibronic peak appearing at 640 nm, the spectrum of the PBTC$_{12}$TPD/PC$_{71}$BM thin film processed in CF incorporating both 0.5 vol% DIO and 1 vol% CN, presented the highest absorption peak intensity among all of our tested films.
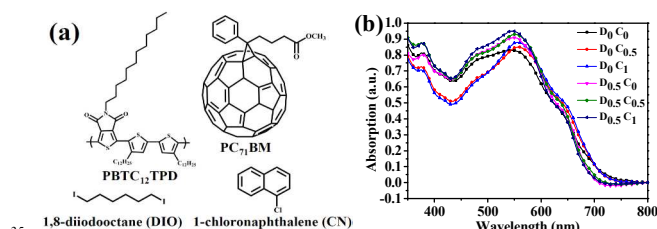
Figure 1. (a) Molecular structures of PBTC$_{12}$TPD, PC$_{71}$BM, and the solvent additives DIO and CN. (b) Absorption spectra of PBTC$_{12}$TPD/PC$_{71}$BM spin-casted films processed in the absence and presence of DIO and CN additives at various volume ratios.

3.2 Photovoltaic Behavior

Figure 2a presents the J–V curves of devices incorporating active layers of PBTC$_{12}$TPD/PC$_{71}$BM that were processed in CF along containing various amounts of the additives. Table 2 presents the corresponding open-circuit voltages (V_{oc}), values of J_{sc}, fill factors (FFs), and PCEs of these devices. The values of V_{oc} of these devices were all in the range 0.90–0.91 V. The control device, D$_0$C$_0$, exhibited a value of J_{sc} of 9.22 mA cm^{-2}, a value of V_{oc} of 0.90 V, an FF of 59% and a PCE of 4.9%. With increasing CN content in the processing solutions, The J_{sc} value increased from 9.76 and 10.10 mA cm^{-2}, respectively for the devices D$_0$C$_{0.5}$ and D$_0$C$_1$. Correspondingly, the PCE increased slightly from 4.9 to 5.3 and to 5.5%. Figure 2b displays the EQEs for the devices

D$_0$C$_0$ to D$_{0.5}$C$_1$. The integrated short-current densities (J_{sc}) deduced from our EQE spectra for the devices D$_0$C$_0$, D$_0$C$_{0.5}$, D$_0$C$_1$, D$_{0.5}$C$_0$, D$_{0.5}$C$_{0.5}$, and D$_{0.5}$C$_1$ were 8.9, 9.4, 9.8, 10.5, 11.3, and 12.2 mA cm^{-2}, respectively. These values (each obtained from the average of ten devices) differ from the correspondingly directly measured J_{sc} by 4% at most, indicating good accuracy in our measurements of device performance. Furthermore, J_{sc} values deduced from the EQE spectra for the devices D$_1$C$_0$, D$_1$C$_{0.5}$, D$_1$C$_1$ were respectively 8.9, 9.7 and 10.2 mA cm^{-2}, as shown in Figure S1.
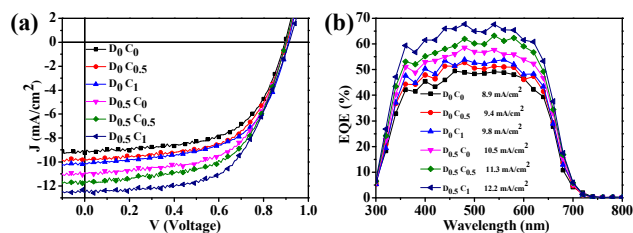
Figure 2. (a) Current density–voltage curves of devices incorporating PBTC$_{12}$TPD/PC$_{71}$BM active layers processed in the presence of various volume ratios of the additives DIO and CN. (b) EQE curves of PBTC$_{12}$TPD/PC$_{71}$BM blend films that had been processed in CF with the incorporation of additives from D$_0$C$_0$ to D$_{0.5}$C$_1$.

The PCE of the device D$_{0.5}$C$_0$ increased to 5.9% from 4.9% for the control device D$_0$C$_0$, along with an increase in the value of J_{sc} to 10.90 from 9.22 mA cm^{-2}. Figure S2 shows that the PCE of the device D$_1$C$_0$ decreased, however, to 4.2% upon further increasing the concentration of DIO in the processing solvent; although DIO is a relatively better solvent for dispersing PC$_{71}$BM clusters, it is a poorer solvent for PBTC$_{12}$TPD when compared with CN (Table 1).

A relatively high concentration of DIO in the processing solvent, such as in the case of device D$_1$C$_0$, resulted in a fill factor (FF) of 50%, lower than that (59%) for the device featuring an active layer processed without any additives. The PCE increased to 5.3% for the device D$_0$C$_{0.5}$ and to 6.2% for D$_{0.5}$C$_{0.5}$, but decreased to 4.6% for D$_1$C$_{0.5}$. We observed the same trend for the cases in which the processing solvent contained 1 vol% CN; increasing the content of DIO to 0.5 vol% increased the PCE of D$_{0.5}$C$_1$ to 6.8% from 5.5% for D$_0$C$_1$, whereas the PCE decreased to 4.8% for D$_1$C$_1$ (i.e., when 1 vol% of DIO and CN were both present in the processing solvent). Overall, the best performance device is D$_{0.5}$C$_1$ with 6.8% PCE and a value of J_{sc} of 12.57 mA cm^{-2}. Further increasing the CN content over 1.0 vol% in the processing solution, with 0.5 vol% DIO, did not improve PCE and J_{sc} values of the hence processed device, implying a saturated CN effect. We have measured and obtained a lower PCE value of 6.2 % for the D$_{0.5}$C$_{1.5}$ device than that for the D$_{0.5}$C$_1$ device, which might be resulted from the unbalanced effect of a high concentration of CN and a low concentration of DIO on the active layer during the processing. All the additive combinations' effect can be explained by the nature and the amount of DIO and CN the boiling point of CN and DIO are 259°C and 333°C, respectively; it indicates that CN had evaporated first after CF (boiling point 61°C) was gone and then followed by the evaporation of DIO−thus this sequence result in the changes of polymer crystallinity and polymer lamellae orientation first and then followed by the refining dispersion of PC$_{71}$BM aggregates. All devices processed with the binary additives, DIO and CN, have been dried in glove box for 12 h and then stayed in vacuum at room-temperature for at least 5 h to completely remove the

residual solvent additives in the active layer prior to evaporation of the back electrode.

Table 2. Averaged (ten devices) photovoltaic characteristics of the devices incorporating $PBTC_{12}TPD/PC_{71}BM$ active layers processed in the presence of various volume ratios of the additives DIO and CN.

Device	Additive concentration (vol%)		V_{oc} (V)	J_{sc} (mA cm^{-2})	FF (%)	PCE (%)
	DIO	CN				
D_0C_0	0	0	0.90 ± 0.01	9.22 ± 0.11	59.1 ± 0.2	4.9 ± 0.13
$D_0C_{0.5}$	0	0.5	0.90 ± 0.02	9.76 ± 0.09	60.6 ± 0.1	5.3 ± 0.20
D_0C_1	0	1	0.91 ± 0.01	10.10 ± 0.15	59.3 ± 0.2	5.5 ± 0.11
$D_{0.5}C_0$	0.5	0	0.90 ± 0.02	10.90 ± 0.11	60.3 ± 0.1	5.9 ± 0.21
$D_{0.5}C_{0.5}$	0.5	0.5	0.90 ± 0.01	11.60 ± 0.09	59.4 ± 0.2	6.2 ± 0.14
$D_{0.5}C_1$	0.5	1	0.91 ± 0.01	12.57 ± 0.08	59.5 ± 0.1	6.8 ± 0.13
D_1C_0	1	0	0.90 ± 0.02	9.30 ± 0.14	50.5 ± 0.2	4.2 ± 0.20
$D_1C_{0.5}$	1	0.5	0.90 ± 0.02	10.12 ± 0.16	50.6 ± 0.3	4.6 ± 0.21
D_1C_1	1	1	0.90 ± 0.01	10.61 ± 0.12	50.5 ± 0.2	4.8 ± 0.15

3.3 Morphological and Crystallinity Study

To decipher the active layer morphology, we used simultaneous GISAXS and GIWAXS for quantitative analysis of the $PC_{71}BM$ cluster size and the extent of $PBTC_{12}TPD$ crystallization and lamellae orientation, respectively. The $PBTC_{12}TPD/PC_{71}BM$ blend films prepared for these X-ray scattering experiments are denoted herein using the same nomenclature as that for device characterization. Figure 3 displays the GISAXS profiles extracted along the in-plane direction, q_y, of the two-dimensional (2D) GISAXS images of the $PBTC_{12}TPD/PC_{71}BM$ blend films processed in CF solutions containing the additives. Figure S4 shows that the intensity of the GISAXS profiles for the blend films increased with the weight ratio of $PC_{71}BM$ (0, 33, 60 to 70 wt%) in the films, suggesting strongly that the weak slope breaks in the GISAXS profiles depend largely on $PC_{71}BM$ aggregation. Hence, these GISAXS profiles are dominated by the aggregation behaviour of $PC_{71}BM$. Moreover, Figure 3a, 3b, and 3c show the GISAXS profiles for the blend films exhibit substantial changes when processed with varying DIO contents; in contrast, relatively minor changes in the GISAXS profiles for the blend films are displayed when processed with varying CN contents. These results are consistent with the preferential solubility of the additives; DIO has a better solubility for $PC_{71}BM$ than CN, and thus presents a more significant effect on $PC_{71}BM$ dispersion than CN in the active layers.
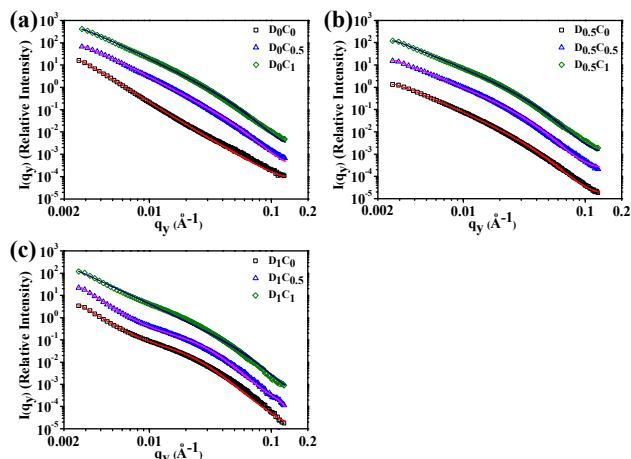
Figure 3. In-plane GISAXS profiles of spin-cast $PBTC_{12}TPD/PC_{71}BM$ films, offset in intensity to show the feature shapes of the profiles that were originally largely overlapped (a) $D_0C_0 \sim D_0C_1$, (b) $D_{0.5}C_0 \sim D_{0.5}C_1$ and (c) $D_1C_0 \sim D_1C_1$, fitted (solid curves) using a fractal-model comprising polydisperse spheres as shown in equation (1).

We determined the $PC_{71}BM$ cluster sizes in these binary additives processed $PBTTPD/PC_{71}BM$ blend films, D_mC_n, by fitting the GISAXS, $I(q_y)$, profiles using a fractal model comprising polydisperse spheres[9,43] that were defined by the following four equations.

$$I(q)=A<P(q)>S(q) \quad\quad\quad\quad\quad (1)$$

The scattering intensity, $I(q)$, is determined by the size-averaged form factor $P(q)$ and structure factor $S(q)$, both of them being functions of scattering vector q, and a scaling parameter A. Since the present GISAXS profiles were measured in relative intensity scales, we have combined all the intensity related factors, such as the scattering contrast and volume fraction, into a single scaling parameter A in the model. The form factor $P(q)$ is proportional to the polydisperse sphere of radius R, as determined in equation (2).[65]

$$P(q) \propto |3j_1(qR)/(qR)|^2 \quad\quad\quad\quad (2)$$

where j_1 is the first order spherical Bessel function. The Schultz size-distribution function, $f(r)$, is defined by equation (3).

$$f(r) = \left(\frac{z+1}{R_a}\right)^{z+1} R^z \exp\left[-\left(\frac{z+1}{R_a}\right)R\right]\frac{1}{\Gamma(z+1)} \quad , \quad z > -1 \quad\quad (3)$$

Where $f(r)$ is a function of the mean radius R_a, width parameter z, and polydispersity $p = (z+1)^{-1/2}$. The fractal structure factor, $S(q)$, is defined in equation (4).

$$S(q) = 1 + \frac{1}{(qR_a)^D}\frac{D\Gamma(D-1)\sin[(D-1)\tan^{-1}(q\xi)]}{[1+(q\xi)^{-2}]^{(D-1)/2}} \quad\quad (4)$$

$S(q)$ describes a fractal structure comprising primary $PC_{71}BM$ aggregates of a mean radius R_a (adapted from the average size of the polydisperse sphere model in our case as an approximation), with the fractal dimension d,[66] and correlation length ξ.[44,67]

Table 3 lists a fitted averaged size of $PC_{71}BM$ fractal cluster of 6.0 nm with a fractal dimension of 2.9 that represents densely packed aggregated $PC_{71}BM$ clusters for the $PBTC_{12}TPD/PC_{71}BM$ film processed without any additive, indicating that $PC_{71}BM$ clusters can easily form large aggregated domains (a fractal

dimension of 3 represents highly dense aggregated $PC_{71}BM$ cluster).

The $PC_{71}BM$ fractal cluster size increased to 8.0 and 8.1 nm with fractal dimension of 2.7 and 2.5 for the $D_0C_{0.5}$ film and
[5] D_0C_1 film, respectively, suggesting that the incorporation of the additive CN in the processing solvent induced larger $PC_{71}BM$ cluster sizes but with lower fullerene packing density. These larger but less densely packed $PC_{71}BM$ clusters can be explained by the speculation that the $PC_{71}BM$ clusters might have been
[10] intercalated by a few $PBTC_{12}TPD$ polymer chains.

When the amount of CN increased while fixing the amount of DIO to be 0.5 vol%, the $PC_{71}BM$ cluster sizes increased to 7.6, 11.0 and 11.2 nm with the corresponding fractal dimension of 2.5, 2.5 and 2.4 for $D_{0.5}C_0$, $D_{0.5}C_{0.5}$ and $D_{0.5}C_1$ films, respectively,
[15] indicating relatively loosely packed $PC_{71}BM$ cluster, as compared to those cases without DIO, as a result of better intermixing between polymer and fullerene.

The $PC_{71}BM$ cluster size increased to 13.2, 13.5 and 14.0 nm with the corresponding fractal dimension of 3.0, 2.9 and 2.7
[20] for D_1C_0, $D_1C_{0.5}$ and D_1C_1 films, respectively. Possibly, the DIO-overcharged binary-additive results in an increasingly larger solubility difference between the $PC_{71}BM$ and the polymer during film drying, leading to larger and less compact $PC_{71}BM$ clusters.

Based on the normalized integrated intensity of (100) peak
[25] in Table 3, the relative population of the face-on polymer lamellae increased with the amount of CN at a fixed amount of DIO while the largest increase in the relative population of the face-on polymer lamellae taking place in the case of 0.5 vol% DIO. This can be explained by the fact that DIO is a relatively
[30] poorer solvent than CN for $PBTC_{12}TPD$ and will lead to diminishing polymer crystallinity when the concentration of DIO increases to 1 vol%.

Figure 4 a and 4b present 2D GIWAXS patterns of the $PBTC_{12}TPD/PC_{71}BM$ films processed with or without the binary
[35] additives ($D_{0.5}C_1$ and D_0C_0 films); we recorded these patterns to correlate the ordering structures of the polymers, corresponding to the edge- and face-on orientation packing of the $PBTC_{12}TPD$ lamellae, relative to the substrate. Figure 4c–4h presents GIWAXS profiles recorded along the out-of-plane (Figure 4c, 4d
[40] and 4e) and in-plane (Figure 4f, 4g and 4h) directions of the $PBTC_{12}TPD/PC_{71}BM$ films processed with and without the additives. Figure 4c displays the profile of the D_0C_0 film, with strong lamellar peaks (100), (200), and (300) located at $q_z = 0.22$, 0.44, and 0.66 Å^{-1}, respectively, due to alkyl stacking,
[45] representing the scattering resulting from the edge-on $PBTC_{12}TPD$ lamellae having an out-of-plane orientation relative to the substrate plane. In addition, an amorphous halo appeared at a value of q_z of 1.41 Å^{-1}, corresponding to the distance between two neighboring fullerene particles, hence, indicating a short-
[50] range ordering of $PC_{71}BM$. The first-order, (100), alkyl stacking peak position was located at a value of q_z of 0.22 Å^{-1} corresponding to a lamellar packing distance of ca. 2.86 nm for the D_0C_0 film; all other D_mC_n films, films processed with different binary additive concentration, show similar crystalline
[55] peaks but with different peak intensities and widths. Figure 4f, 4g, and 4h show the (100) peak for face-on lamellae in the GIWAXS profiles change with the variation of CN content in the processing solvent. To quantitatively determine the CN additive effects, we calculate the integrated intensities of the (100) peaks of $I(q_z)$ and
[60] $I(q_y)$ for the edge-on and face-on $PBTC_{12}TPD$ lamellae, respectively, from the GIWAXS profiles; from the (100) peak widths, the corresponding approximately crystal dimensions (or correlation lengths) are also deduced based on the Scherrer equation for comparison.[10,44,56,68] We note that the presented
[65] GIWAXS profiles along the out-of-plane direction of the film in

Figure 4 c-h are extracted directly from the 2D GIWAXS patterns before pole-figure corrections.[69] Nevertheless, the GIWAXS 2D patterns corrected for pole figures have contained missing wedges along the q_z (Figure 4a and 4b), as detailed in a previous
[70] report.[69] Hence, the presented GIWAXS profiles along q_z (obtained from the original 2D GIWAXS patterns) represent only approximately the diffraction intensity from upright edge-on lamellae. To remedy this approximation, we have carried out X-ray diffraction (XRD) measurement on a D_0C_0 film for a
[75] diffraction $I(q_z)$ profile from upright edge-on crystalline lamellae.[69] Figure S5 shows the XRD profile is consistent with the GIWAXS profile, particularly in the low-q_z region for the (100) peak. Nevertheless, the (100) peak width from the GIWAXS profile is about 25% larger than that from the XRD
[80] profile (0.046 vs. 0.037 A^{-1}). We, therefore, systemically increase all the crystal domain sizes extracted from the GIWAXS (100) peak width by 25% for the edge-on polymer lamellae. Table 3 summarizes the results; we note that the size correction would not alter the relative trend of crystallization behavior for these D_mC_n
[85] films.
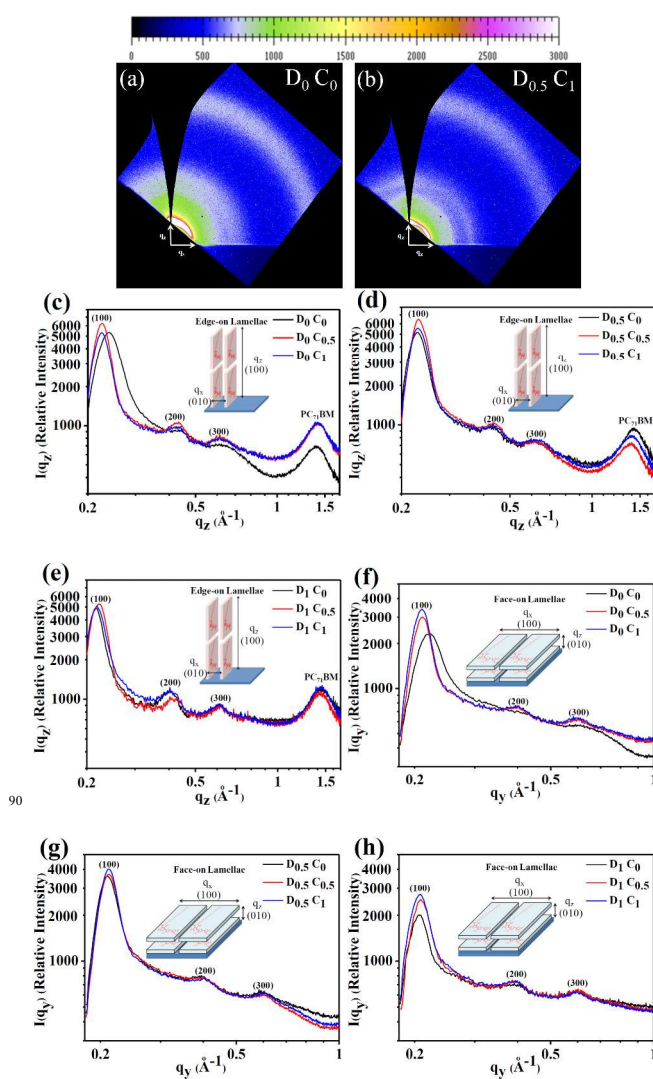
Figure 4. Pole figures of the 2D GIWAXS patterns of (a) D_0C_0 and (b) $D_{0.5}C_1$. Corresponding out-of-plane GIWAXS profiles of (c) D_0C_0 to D_0C_1, (d) $D_{0.5}C_0$ to $D_{0.5}C_1$ and (e) D_1C_0 to D_1C_1 and
[95] in-plane GIWAXS profiles of (f) D_0C_0 to D_0C_1, (g) $D_{0.5}C_0$ to

$D_{0.5}C_1$ and (h) D_1C_0 to D_1C_1 from the spin-cast $PBTC_{12}TPD/PC_{71}BM$ films.

Table 3 lists the normalized integrated intensity, $q_{z\text{-}100}$ and $q_{y\text{-}100}$, of (100) peak $I(q_z)$ and $I(q_y)$ of the edge- and face-on
5 $PBTC_{12}TPD$ lamellae for all the D_nC_m films. For comparison convenience, we have normalized the $q_{z\text{-}100}$ and $q_{y\text{-}100}$ values for all samples by the $q_{z\text{-}100}$ of the D_0C_0 film. Table 3 shows that when the CN concentration increased from 0 to 1% while the volume concentration of DIO being kept at 0.5%, similar
10 $PC_{71}BM$ dispersions ($d \sim$ 2.4-2.5 and $2R_a \sim$ 7.6-11.2 nm) occurred in the blend films, but the normalized integrated intensity of (100) peaks of the face-on lamellae increase more than 25% (48 vs. 38), relative to that of the D_0C_0 film. As a result of better fullerene dispersions (less fullerene aggregation) and
15 higher population of face-on $PBTC_{12}TPD$ lamellae in the case of binary additives, as compared to the case without any additive, the PCE values are enhanced to 5.9, 6.2, and 6.8% for the $D_{0.5}C_0$, $D_{0.5}C_{0.5}$, and $D_{0.5}C_1$ devices, respectively, from 4.9% for the D_0C_0 device. Table 3 also reveals that increasing the concentration of
20 DIO from 0.5 to 1 vol% led to significant decreases in the population of both the edge- and face-on polymer lamellae, implying that a content of DIO of 1 vol% was too high and could interfere the polymer $PBTC_{12}TPD$ crystallization in the processing solvent (CF). Table 3 also lists the calculated
25 dimensions of $PBTC_{12}TPD$ (100) edge- and face-on lamellar crystal using the Scherrer equation.[68] The introduction of additives (DIO, CN, or DIO + CN) enhanced the edge- and face-on lamellae sizes to 24 nm and 23 nm from 16 and 15 nm, respectively, 50 and 53% increases, respectively, relative to those
30 in the pristine film. Hence, using DIO and CN as binary additives, we can simultaneously reduce the size of $PC_{71}BM$ aggregate domains and tune the relative orientation of the $PBTC_{12}TPD$ lamellae.

Table 3. Structural parameters of $PBTC_{12}TPD/PC_{71}BM$ films
35 processed with and without additives.

Notation	$2R_a{}^a$ (nm)	d^b	$q_{z\text{-}100}{}^c$ (edge-on lamellae) (%)	L (nm)^d (edge-on)	$q_{y\text{-}100}{}^c$ (face-on lamellae) (%)	L (nm)^d (face-on)
D_0C_0 film	6.0 ± 0.55	2.9 ± 0.019	100	16	38	15
$D_0C_{0.5}$ film	8.0 ± 0.62	2.7 ± 0.027	87	23	38	22
D_0C_1 film	8.1 ± 0.58	2.5 ± 0.025	77	23	41	22
$D_{0.5}C_0$ film	7.6 ± 0.47	2.5 ± 0.028	85	23	45	21
$D_{0.5}C_{0.5}$ film	11.0 ± 0.53	2.5 ± 0.036	95	21	46	20
$D_{0.5}C_1$ film	11.2 ± 0.56	2.4 ± 0.029	88	20	48	22
D_1C_0 film	13.2 ± 0.57	~3.0 ± 0.014	62	24	30	23
$D_1C_{0.5}$ film	13.5 ± 0.63	2.9 ± 0.023	69	21	34	20
D_1C_1 film	14.0 ± 0.61	2.7 ± 0.038	70	23	36	21

^{a} $2R_a$: Average size of $PC_{71}BM$ clusters.
^{b} d: Fractal dimension.
^{c} Normalized integrated intensity of (100) peak for $q_{z\text{-}100}$ and $q_{y\text{-}100}$.
^{d} L: Edge-on (or face-on) lamellar size of the conjugated polymer.

Figure 5 summarizes the results of our GISAXS and GIWAXS studies. The result suggests that lamellar crystallites having an edge-on orientation might partially reorient to a face-on arrangement, as increases of the volume percentages of DIO
45 and CN. We suggest that the binary additives might affect the polarity between the substrate surface and the linear alkyl chains of $PBTC_{12}TPD$, thereby changing the polymer's preferred orientation into a face-on arrangement, particularly when the additive concentrations are high. Through the use of the binary
50 additives, we not only can modulate a large $PC_{71}BM$ fractal structure network (domain) that comprises many closely pack $PC_{71}BM$ clusters to smaller aggregated $PC_{71}BM$ domains that consist of more appropriated $PC_{71}BM$ cluster size (11 nm) of a lower fractal dimension but also induce an increase in the
55 population of the face-on polymer lamellae at the expense of the edge-on polymer lamellae, resulting in a more isotropic orientation, as compared to the case of without any additive. A combination of more appropriated $PC_{71}BM$ cluster size and higher population of the face-on polymer lamellae can lead to
60 superior pathways for carrier transport. Thus, Figure 5 shows the PCE value was enhanced to 6.8% for the $D_{0.5}C_1$ device with an active layer comprising an appropriated $PC_{71}BM$ cluster size with a fractal dimension of 2.4 and the face-on polymer lamellae intensity of 48 from 4.9% for the D_0C_0 device with an active
65 layer comprising a large $PC_{71}BM$ fractal structure network with a fractal dimension of 2.9 and the face-on polymer lamellae intensity of 38.
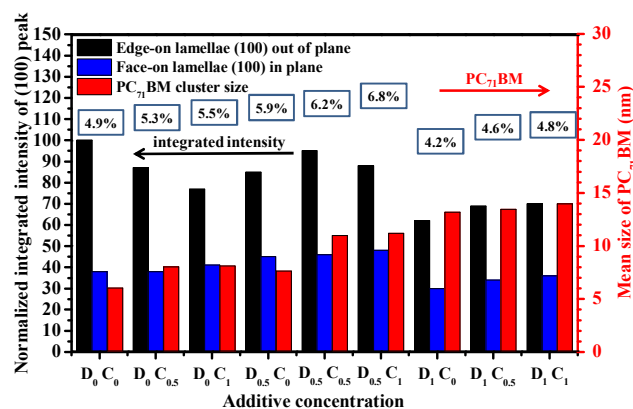
Figure 5. Normalized integrated intensity of (100) peak of the
70 edge- and face-on lamellae and $PC_{71}BM$ cluster size in the $PBTC_{12}TPD/PC_{71}BM$ films processed with additives, ranging from D_0C_0 to D_1C_1.

We also qualitatively determine the degree of molecular-scale intermixing between the polymer and fullerene with
75 photoluminescence (PL) and time-resolved PL (TRPL) spectra. Figure 6 shows the PL and TRPL spectra of the $PBTC_{12}TPD/PC_{71}BM$ films, and the inset shows that the intensity of the PL peak at 833 nm for the case of $D_{0.5}C_1$ film (processed with 0.5 vol% DIO and 1 vol% CN) is quenched, as compared to
80 that for the case of D_0C_0 film (processed without any additive), indicating that the extent of charge recombination is reduced, and thus have more excitons available for dissociation. Moreover, Figure 6 displays a faster decay of the transient PL peak for the $D_{0.5}C_1$ film than that for the D_0C_0 film, revealing a slightly
85 shorter exciton life time for $D_{0.5}C_1$ film than for the D_0C_0 film (τ_c = 0.27 ns vs. τ_c = 0.32 ns). A shorter exciton life time suggests possibly a better molecule-scale intermixing between the fullerene and polymer, as facilitated by the additives used.[15,16]

The PL and TRPL results are consistent with the GISAXS result that the binary additives enhanced more homogeneous dispersion of the $PC_{71}BM$ in the polymer.
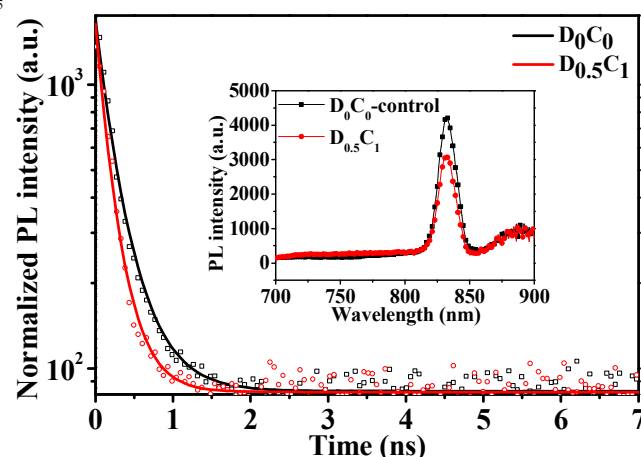
Figure 6. Time-resolved photoluminescence (TRPL) spectra, detected with an 833-nm laser for the D_0C_0 and $D_{0.5}C_1$ films. The wavelength 833 nm was chosen premeditatedly owing to a PBTC$_{12}$TPD-dominated PL (absorption) intensity (inset). The PBTC$_{12}$TPD-dominated exciton lifetimes (τ_e) are comparable (0.32 ns vs. 0.27 ns). The inset is the corresponding PL spectra excited with 550 nm laser.

Figure 7 presents the top-view TEM images of the D_0C_0 and $D_{0.5}C_1$ films, respectively. For the D_0C_0 film processed without additives, Figure 7a reveals bright and dark regions representing the conjugated polymer- and fullerene-rich domains, respectively, arising from the large difference in electron scattering density between the fullerene (1.5 g cm^{-3}) and the polymer (1.1 g cm^{-1}); large $PC_{71}BM$ aggregated domains (average diameter size: ca. 150 nm; mean spacing: ca. 210 nm) were present. In Figure 7b, we observe that the $PC_{71}BM$ aggregated domains in the $D_{0.5}C_1$ film had decreased dramatically (to ca. 40 nm). Based on our GISAXS fitting results and TEM images, we noted that for the case of without any additive, D_0C_0, the large aggregated $PC_{71}BM$ domains (150 nm) comprise individual $PC_{71}BM$ molecule (cluster) that are densely packed (fractal dimension 2.9). The size of aggregated $PC_{71}BM$ domains become much smaller and the $PC_{71}BM$ clusters become more porous (2.4) for the case of $D_{0.5}C_1$. When the DIO concentration increased to a critical concentration of 1 vol% in the binary additives, the $PC_{71}BM$ clusters become highly packed.
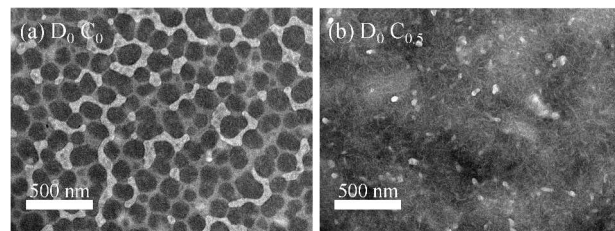
Figure 7. TEM images of PBTC$_{12}$TPD/$PC_{71}BM$ films prepared (a) in the absence of additives and (b) in the presence of 0.5 vol% DIO and 1 vol% CN in the processing solvent.

Figure S3 shows the TEM images for other D_nC_m films. The film morphology is relatively more homogenous without large domain boundary, compared to the D_0C_0 film; these may correspond to the larger fractal network (larger correlation length;

cf. Table S1) formed by the better disperse (lower fractal dimension) PCBM aggregates, revealed from GISAXS.

Figure 8 presents the cartoon images of the PBTC$_{12}$TPD/$PC_{71}BM$ morphologies that are consistent with the structural information we obtained from the GISAXS, GIWAXS, and TEM analyses. We found that the optimal ratio of the binary additives enhanced the population of polymer face-on lamellae, at the expense of slightly depressed population of the edge-on lamellae, while modulating $PC_{71}BM$ clusters for forming lower dimension fractal structure ($d \approx 2.4$) with appropriate primary aggregate size of 11 nm. We note that the lower fractal dimension also suggest a better intermixed $PC_{71}BM$ and polymer in the matrix (acting as the third phase), as also illustrated in the cartoons. The possible role of the third phase that comprised well-mixed $PC_{71}BM$ and polymer has been discussed extensively.[23,24] This well-mixed phase associates implicitly with the packing of $PC_{71}BM$ and the crystallinity of the polymer that were determined from GISAXS and GIWAXS, respectively, due to conservation of the total volume. Better miscibility between $PC_{71}BM$ and polymer results in a larger matrix phase, presumably corresponding to smaller domains of $PC_{71}BM$ aggregates and polymer crystallites.
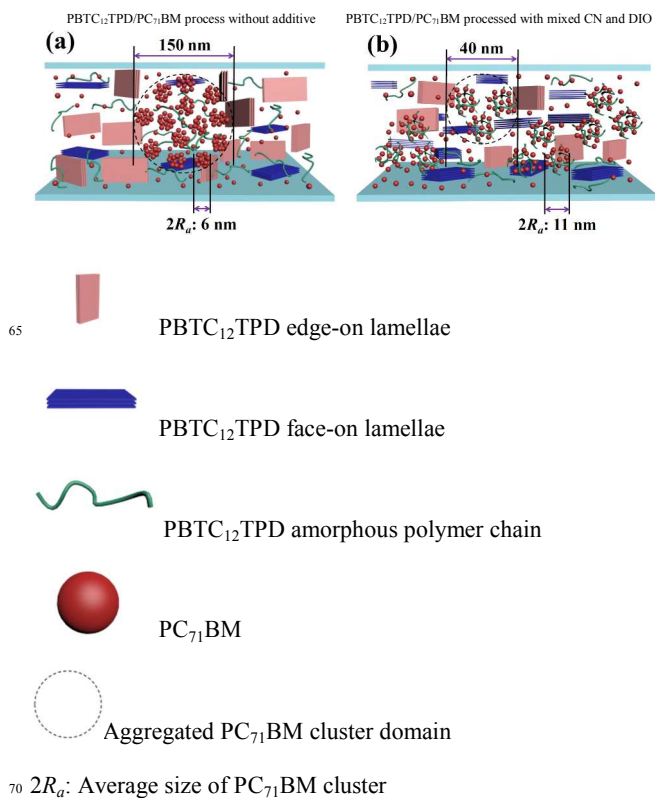
Figure 8. Schematic representation of polymer lamellae with edge-on and face-on orientations and fractal-like $PC_{71}BM$ clusters in spin-cast PBTC$_{12}$TPD/$PC_{71}BM$ films that were processed: (a) in the absence of additives and (b) in the presence of a mixture of DIO and CN. (this figure is not proportional to the real scale)

4. Conclusions

CN and DIO have relative preferential solubility for PBTC$_{12}$TPD and $PC_{71}BM$, respectively, and therefore can tune the orientation

of polymer lamellae and the degree of dispersion of $PC_{71}BM$ in $PBTC_{12}TPD/PC_{71}BM$ films, prepared from CF solutions containing these additives. We examined the resulting morphologies of these films through GISAXS/GIWAXS and TEM characterizations and concluded that DIO can effectively modulate the size of the fractal-like $PC_{71}BM$ clusters and their aggregated domains while CN can induce higher population of face-on polymer lamellae under proper binary additive concentrations. Correspondingly, an improvement in device performance with a PCE of 6.8% could be achieved with a device incorporating a $PBTC_{12}TPD/PC_{71}BM$ thin film deposited with 0.5 vol% DIO and 1 vol% CN as additives in the processing solvent. Presumably, this combination of additives provided a more balanced solubility between the polymer and the fullerene, resulting in an optimized degree of phase separation in the active layer, as compared to the case without any additive. In conclusion, the binary additives approach leads to a better active layer morphology that combines the suitable polymer lamellae orientation and better fullerenes dispersion, resulting in an increase in the generated photocurrent because of more efficient exciton dissociation and better carrier transport pathway and, therefore, leading to enhanced PCE, as compared to the case without additive.

Acknowledgements

Notes and references

[a] Department of Materials Science and Engineering, National Chiao Tung University, 1001 Ta Hsueh Road, Hsinchu 30010, Taiwan. E-mail: khwei@mail.nctu.edu.tw; Tel: +886-3-5712121 ext:31871
[b] National Synchrotron Radiation Research Center 101 Hsin-Ann Road, Science-Based Industrial Park Hsinchu 30077, Taiwan. E-mail: usjeng@nsrrc.org.tw; Tel: +886-3-5780281 ext:7108
[c] Department of Chemical Engineering, National Tsing Hua University, Hsinchu 30013, Taiwan.

†Electronic Supplementary Information (ESI) available: [details of any supplementary information available should be included here]. See DOI: 10.1039/b000000x/

1   G. Li, R. Zhu and Y. Yang, *Nat. Photonics* 2012, **6**, 153−161.
2   J. A. Bartelt, J. D. Douglas, W. R. Mateker, A. E. Labban, C. J. Tassone, M. F. Toney, J. M. J. Fréchet, P. M. Beaujuge and M. D. McGehee, *Adv. Energy Mater.* 2014, 1301733.
3   J. M. Jiang, M. C. Yuan, K. Dinakaran, A. Hariharan and K. H. Wei, *J. Mater. Chem. A* 2013, **1**, 4415−4422.
4   J. Peet, A. J. Heeger, and C. G. Bazan, *Acc. Chem. Res.* 2009, **42**, 1700−1708.
5   B. C. Thompson and J. M. J. Fréchet, *Angew. Chemie Int. Ed.* 2008, **120**, 62−82.
6   Y. W. Su, S. C. Lan and K. H. Wei, *Mater. Today* 2012, **15**, 554−562.
7   J. M. Jiang, P. Raghunath, H. K. Lin, Y. C. Lin, M. C. Lin, and K. H. Wei, *Macromolecules* 2014, DOI: 10.1021/ma501720k.
8   M. Pfaff, P. Muller, P. Bockstaller, E. Muller, J. Subbiah, W. W. H. Wong, M. F. G. Klein, S. R. Puniredd, W. Pisula, A. Colsmann, D. Gerthsen and D. J. Jones, *ACS Appl. Mater. Interfaces* 2013, **5**, 11554−11562.
9   C. M. Liu, C. M. Chen, Y. W. Su, S. M. Wang and K. H. Wei, *Org. Electron.* 2013, **14**, 2476−2483.
10 M. S. Su, C. Y. Kuo, M. C. Yuan, U. S. Jeng, C. J. Su and K. H. Wei, *Adv. Mater.* **2011,** *23*, 3315−3319.
11 C. M. Liu, M. S. Su, J. M. Jiang, Y. W. Su, C. J. Su, C. Y. Chen, C. S. Tsao and K. H. Wei, *ACS Appl. Mater. Interfaces* 2013, **5**, 5413−5422.
12 Y. Gu, C. Wang and T. P. Russell, *Adv. Energy Mater.* **2012,** *2*, 683−690.
13 M. Kim, J. H. Kim, H. H. Choi, J. H. Park, S. B. Jo, M. Sim, J. S. Kim, H. Jinnai, Y. D. Park and K. Cho, *Adv. Energy Mater.* 2014, **4**, 1300612.
14 C. J. Schaffer, C. M. Palumbiny, M. A. Niedermeier, C. Jendrzejewski, G. Santoro, S. V. Roth and P. Müller-Buschbaum, *Adv. Mater.* 2013, **25**, 6760–6764.
15 E. T. Hoke, K. Vandewal, J. A. Bartelt, W. R. Mateker, J. D. Douglas, R. Noriega, K. R. Graham, J. M. J. Fréchet, A. Salleo and M. D. McGehee, *Adv. Energy Mater.* 2013, **3**, 220−230.
16 G. J. Hedley, A. J. Ward, A. Alekseev, C. T. Howells, E. R. Martins, L. A. Serrano, G. Cooke, A. Ruseckas and I. D. W. Samuel, *Nat. Commun.* 2013, **4**, 2867.
17 Z. M. Beiley, E. T. Hoke, R. Noriega, J. Dacuña, G. F. Burkhard, J. A. Bartelt, A. Salleo, M. F. Toney and M. D. McGehee, *Adv. Energy Mater.* 2011, **1**, 954−962.
18 T. Wang, A. J. Pearson, A. D. F. Dunbar, P. A. Staniec, D. C. Watters, H. Yi, A. J. Ryan, R. A. L. Jones, A. Iraqi and D. G. Lidzey, *Adv. Funct. Mater.* 2012, **22**, 1399–1408.
19 M. Y. Chiu, U. S. Jeng, C. H. Su, K. S. Liang and K. H. Wei, *Adv. Mater.* 2008, **20**, 2573–2578.
20 P. Kohn, Z. Rong, K. H. Scherer, A. Sepe, M. Sommer, P. Müller-Buschbaum, R. H. Friend, U. Steiner and S. Hüttner, *Macromolecules* 2013, **46**, 4002−4013.
21 S. B. Darling and F. You, *RSC Adv.* 2013, **3**, 17633–17648.
22 W. Chen, M. P. Nikiforov and S. B. Darling, *Energy Environ. Sci.* 2012, **5**, 8045–8074.
23 G. Kaune, E. Metwalli, R. Meier, V. Korstgens, K. Schlage, S. Couet, R. Rohlsberger, S. V. Roth and P. Muller-Buschbaum, *ACS Appl. Mater. Interfaces* 2011, **3**, 1055–1062.
24 S. Yu, G. Santoro, K. Sarkar, B. Dicke, P. Wessels, S. Bommel, R. Döhrmann, J. Perlich, M. Kuhlmann, E. Metwalli, J. F. H. Risch, M. Schwartzkopf, M. Drescher, P. Müller-Buschbaum and S. V. Roth, *J. Phys. Chem. Lett.* 2013, **4**, 3170−3175.
25 X. Guo, N. Zhou, S. J. Lou, J. Smith, D. B. Tice, J. W. Hennek, R. P. Ortiz, J. T. L. Navarrete, S. Li, J. Strzalka, L. X. Chen, R. P. H. Chang, A. Facchetti and T. J. Marks, *Nat. Photonics* 2013, **7**, 825−833.
26 M. T. Dang and J. D. Wuest, *Chem. Soc. Rev.* 2013, **42**, 9105−9126.
27 F. Liu, C. Wang, J. K. Baral, L. Zhang, J. J. Watkins, A. L. Briseno and T. P. Russell, *J. Am. Chem. Soc.* 2013, **135**, 19248−19259.
28 J. Peet, J. Y. Kim, N. E. Coates, W. L. Ma, D. Moses, A. J. Heeger and G. C. Bazan, *Nat. Mater.* 2007, **6**, 497−500.
29 C. Piliego, T. W. Holcombe, J. D. Douglas, C. H. Woo, P. M. Beaujuge and J. M. J. Fréchet, *J. Am. Chem. Soc.* 2010, **132**, 7595−7597.

30 J. K. Lee, W. L. Ma, C. J. Brabec, J. Yuen, J. S. Moon, J. Y. Kim, K. Lee, G. C. Bazan and A. J. Heeger, *J. Am. Chem. Soc.* 2008, **130**, 3619−3623.

31 C. V. Hoven, X. D. Dang, R. C. Coffin, J. Peet, T. Q. Nguyen and G. C. Bazan, *Adv. Mater.* 2010, **22**, E63−66.

32 C. H. Woo, P. M. Beaujuge, T. W. Holcombe, O. P. Lee and J. M. J. Fréchet, *J. Am. Chem. Soc.* 2010, **132**, 15547−15549.

33 P. Cheng, L. Ye, X. Zhao, J. Hou, Y. Li and X. Zhan, *Energy Environ. Sci.* 2014, **7**, 1351−1356.

34 J. Jo, J. R. Pouliot, D. Wynands, S. D. Collins, J. Y. Kim, T. L. Nguyen, H. Y. Woo, Y. Sun, M. Leclerc and A. J. Heeger, *Adv. Mater.* 2013, **25**, 4783−4788.

35 B. R. Aïch, J. Lu, S. Beaupré, M. Leclerc and Y. Tao, *Org. Electron.* 2012, **13**, 1736−1741.

36 I. Osaka, T. Kakara, N. Takemura, T. Koganezawa and K. Takimiya, *J. Am. Chem. Soc.* 2013, **135**, 8834−8837.

37 A. C. Stuart, J. R. Tumbleston, H. Zhou, W. Li, S. Liu, H. Ade, W. You, *J. Am. Chem. Soc.* 2013, **135**, 1806−1815.

38 M. S. Chen, J. R. Niskala, D. A. Unruh, C. K. Chu, O. P. Lee and J. M. J. Fréchet, *Chem. Mater.* 2013, **25**, 4088−4096.

39 L. A. Perez, P. Zalar, L. Ying, K. Schmidt, M. F. Toney, T. Q. Nguyen, G. C. Bazan and E. J. Kramer, *Macromolecules* 2014, **47**, 1403−1410.

40 J. Guo, Y. Liang, J. Szarko, B. Lee, H. J. Son, B. S. Rolczynski, L. Yu and L. X. Chen, *J. Phys. Chem. B* 2009, **114**, 742−748.

41 M. R. Hammond, R. J. Kline, A. A. Herzing, L. J. Richter, D. S. Germack, H. W. Ro, C. L. Soles, D. A. Fischer, T. Xu, L. Yu, M. F. Toney and D. M. DeLongchamp, *ACS Nano* 2011, **5**, 8248−8257.

42 K. Schmidt, C. J. Tassone, J. R. Niskala, A. T. Yiu, O. P. Lee, T. M. Weiss, C. Wang, J. M. J. Fréchet, P. M. Beaujuge and M. F. Toney, *Adv. Mater.* 2014, **26**, 300−305.

43 W. Ma, J. R. Tumbleston, L. Ye, C. Wang, J. H. Hou and H. Ade, *Adv. Mater.* 2014, **26**, 4234–4241.

44 W. R. Wu, U. S. Jeng, C. J. Su, K. H. Wei, M. S. Su, M. Y. Chiu, C. Y. Chen, W. B. Su, C. H. Su and A. C. Su, *ACS Nano* 2011, **5**, 6233−6243.

45 B. Schmidt-Hansberg, M. Sanyal, M. F. G. Klein, M. Pfaff, N. Schnabel, S. Jaiser, A. Vorobiev, E. Müller, A. Colsmann, P. Scharfer, D. Gerthsen, U. Lemmer, E. Barrena and W. Schabel, *ACS Nano* 2011, **5**, 8579−8590.

46 A. J. Pearson, T. Wang, A. D. F. Dunbar, H. Yi, D. C. Watters, D. M. Coles, P. A. Staniec, A. Iraqi, R. A. L. Jones and D. G. Lidzey, *Adv. Funct. Mater.* 2014, **24**, 659−667.

47 K. W. Chou, B. Yan, R. Li, E. Q. Li, K. Zhao, D. H. Anjum, S. Alvarez, R. Gassaway, A. Biocca, S. T. Thoroddsen, A. Hexemer and A. Amassian, *Adv. Mater.* 2013, **25**, 1923−1929.

48 S. J. Lou, J. M. Szarko, T. Xu, L. Yu, T. J. Marks and L. X. Chen, *J. Am. Chem. Soc.* 2011, **133**, 20661−20663.

49 J. T. Rogers, K. Schmidt, M. F. Toney, G. C. Bazan and E. J. Kramer, *J. Am. Chem. Soc.* 2012, **134**, 2884−2887.

50 S. Guo, E. M. Herzig, A. Naumann, G. Tainter, J. Perlich and P. Muller-Buschbaum, *J. Phys. Chem. B* 2014, **118**, 344−350.

51 C. S. Tsao and H. L. Chen, *Macromolecules* 2004, **37**, 8984−8991.

52 H. C. Liao, C. C. Ho, C. Y. Chang, M. H. Jao, S. B. Darling and W. F. Su, *Mater. Today* 2013, **16**, 326−336.

53 P. Müller-Buschbaum, *Anal. Bioanal. Chem.* 2003, **376**, 3–10.

54 H. C. Liao, C. S. Tsao, T. H. Lin, C. M. Chuang, C. Y. Chen, U. S. Jeng, C. H. Su, Y. F. Chen and W. F. Su, *J. Am. Chem. Soc.* 2011, **133**, 13064–13073.

55 M. Y. Chiu, U. S. Jeng, M. S. Su and K. H. Wei, *Macromolecules* 2010, **43**, 428–432.

56 F. Liu, Y. Gu, X. Shen, S. Ferdous, H. W. Wang and T. P. Russell, *Prog. Polym. Sci.* 2013, **38**, 1990–2052.

57 J. Perlich, J. Rubeck, S. Botta, R. Gehrke, S. V. Roth, M. A. Ruderer, S. M. Prams, M. Rawolle, Q. Zhong, V. Körstgens and P. Müller-Buschbaum, *Rev. Sci. Instrum.* 2010, **81**, 105105.

58 C. H. Hsu, U. S. Jeng, H. Y. Lee, C. M. Huang, K. S. Liang, D. Windover, T. M. Lu and C. Jin, *Thin Solid Films* 2005, **472**, 323–327.

59 C. M. Palumbiny, C. Heller, C. J. Schaffer, V. Körstgens, G. Santoro, S. V. Roth, and P. Müller-Buschbaum, *J. Phys. Chem. C* 2014, **118**, 13598–13606.

60 F. Liu, Y. Gu, C. Wang, W. Zhao, D. Chen, A. L. Briseno and T. P. Russell, *Adv. Mater.* 2012, **24**, 3947−3951.

61 J. W. Jung, F. Liu, T. P. Russell and W. H. Jo, *Chem. Commun.* 2013, **49**, 8495−8497.

62 J. T. Rogers, K. Schmidt, M. F. Toney, E. J. Kramer and G. C. Bazan, *Adv. Mater.* 2011, **23**, 2284−2288.

63 M. C. Yuan, M. Y. Chiu, S. P. Liu, C. M. Chen and K. H. Wei, *Macromolecules* 2010, **43**, 6936−6938.

64 U. S. Jeng, C. H. Su, C. J. Su, K. F. Liao, W. T. Chuang, Y. H. Lai, J. W. Chang, Y. J. Chen, Y. S. Huang, M. T. Lee, K. L. Yu, J. M. Lin, D. G. Liu, C. F. Chang, C. Y. Liu, C. H. Chang and K. S. Liang, *J. Appl. Cryst.* 2010, **43**, 110−121.

65 U. S. Jeng, Y. S. Sun, H. Y. Lee, C. H. Hsu, K. S. Liang, S. W. Yeh and K. H. Wei, *Macromolecules* 2004, **37**, 4617−4622.

66 U. S. Jeng, W. J. Liu, T. L. Lin, L. Y. Wang and L. Y. Chiang, *Fullerene Sci. Technol.* 1999, **7**, 599–606.

67 J. M. Lin, T. L. Lin, U. S. Jeng, Z. H. Huang and Y. S. Huang, *Soft Matter* 2009, **5**, 3913–3919.

68 C. R. Singh, G. Gupta, R. Lohwasser, S. Engmann, J. Balko, M. Thelakkat, T. Thurn-Albrecht, H. Hoppe, *J. Polym. Sci., Part B: Polym. Phys.* 2013, **51**, 943−951.

69 J. L. Baker, L. H. Jimison, S. Mannsfeld, S. Volkman, S. Yin, V. Subramanian, A. Salleo, A. P. Alivisatos and M. F. Toney, *Langmuir* 2010, **26**, 9146−9151.

Table of Contents

The binary additives approach lead to a better active layer that combines the face-on polymer lamellae and finer fullerenes dispersion.